PCCP

PERSPECTIVE

Practical applications of small-angle neutron scattering

Martin J. Hollamby*

Recent improvements in beam-line accessibility and technology have led to small-angle neutron scattering (SANS) becoming more frequently applied to materials problems. SANS has been used to study the assembly, dispersion, alignment and mixing of nanoscale condensed matter, as well as to characterise the internal structure of organic thin films, porous structures and inclusions within steel. Using time-resolved SANS, growth mechanisms in materials systems and soft matter phase transitions can also be explored. This review is intended for newcomers to SANS as well as experts. Therefore, the basic knowledge required for its use is first summarised. After this introduction, various examples are given of the types of soft and hard matter that have been studied by SANS. The information that can be extracted from the data is highlighted, alongside the methods used to obtain it. In addition to presenting the findings, explanations are provided on how the SANS measurements were optimised, such as the use of contrast variation to highlight specific parts of a structure. Emphasis is placed on the use of complementary techniques to improve data quality (*e.g.* using other scattering methods) and the accuracy of data analysis (*e.g.* using microscopy to separately determine shape and size). This is done with a view to providing guidance on how best to design and analyse future SANS measurements on materials not listed below.

International Center for Young Scientists (ICYS), National Institute for
Materials Science (NIMS), 1-2-1 Sengen, Tsukuba, 305-0047 Japan.
E-mail: Hollamby.martinjames@nims.go.jp, mjhollamby@gmail.com

Dr Martin Hollamby is a Researcher in the International Center for Young Scientists, National Institute of Materials Science (NIMS), Tsukuba, Japan. He received his PhD at the University of Bristol, UK, working in the group of Professor J. Eastoe and studying the use of SANS to characterise surfactant self-assemblies in unusual solvents such as fluorocarbons and liquid CO₂. In 2009 he moved to the Max-Planck

Martin J. Hollamby

Institute of Colloids and Interfaces, Potsdam-Golm, Germany, working with Prof. H. Möhwald and in 2011 was awarded a JSPS postdoctoral fellowship to work in NIMS with Dr T. Nakanishi. His research focuses on molecular self-assembly for organic electronics, and the application of scattering techniques, including SANS, for characterising the structure and formation mechanisms of condensed matter. From the end of May 2013, he will start a Lectureship at Keele University, UK.

1. Introduction

Small-angle scattering is a powerful analysis tool, capable of selectively resolving structures of the order 1 nm to over 100 nm. As such, it has been applied to topics ranging from soft materials, such as molecular self-assemblies and gels, to hard or porous structures and precipitates in steels. One major advantage is the ability to determine a statistically significant bulk average particle size. Measurable sample volumes are typically 10–100 mm³ for SANS and as such, a vast number of scatterers can be probed in a single experiment. For example, over 10^{14} particles occupy a 10 mm³ sample if their average diameter is 10 nm and concentration is 1 vol%. Imaging such a number using microscopy would be inconceivable, even with the aid of image analysis software.

In addition, scattering techniques can visualise the internal structure of materials *in situ*, for example in solution in capillaries, at elevated temperatures, under pressure, applied load or in the presence of an external magnetic field (*vide infra*). The ability to do this removes the need for pre-treatment steps such as drying, freezing or sectioning that may otherwise perturb a sample. In this respect, neutrons have particular advantages over X-rays (SAXS), having a larger penetration depth and not suffering from issues of sample beam damage. Furthermore, using contrast variation SANS, different parts of a sample can be selectively highlighted *via* isotopic labelling,

for example by exchanging hydrogen (^{1}H) for deuterium (^{2}D). These latter benefits are particularly applicable to hydrogen-rich organic or biological materials. Consequently, SANS is often used to study these systems.

On the other hand, SANS suffers several disadvantages that have perhaps limited its more widespread application. The first of these is a historical problem with access, although over the past years direct access schemes such as those run by ISIS, UK have addressed this issue. Additionally, the low flux of neutron sources in comparison to X-ray sources means that longer measurement times are necessary to obtain statistically reasonable data. Most problematic of all though, may be the lack of familiarity outside the scattering community of the general abilities of small-angle scattering. This is compounded by the relative complexity of data analysis in comparison to more visual microscopy techniques.

Building on the excellent work of others,[1–8] this perspective highlights the myriad ways in which SANS has recently been used to tackle materials science problems. Alongside this, a brief introduction to the basics of the technique is given, including an assessment of the best ways to design, enact and analyse data from SANS experiments. The examples are chosen to show the diversity of SANS, with the view to provoking ideas and future studies. While the focus here is on the use of normal SANS, the complementary use of X-rays[9,10] and/or ultra-SANS (USANS)[11,12] will be explored, as combining these techniques can be a powerful way to unambiguously characterise a system.

1.1 Scattering basics

Many comprehensive introductions to small-angle scattering have been published elsewhere, most of which are freely available online.[9,10,13–16] Rather than repeating that material, this section aims to give a brief introduction to the basics, a knowledge of which can help in designing suitable experiments, and in understanding the results obtained. In general, small-angle scattering derives from an interaction between the incident radiation and structures within a sample, for example molecular assemblies or nanoparticles. Typically, the scattered intensity, $I(Q)$ is reported as a function of the scattering vector, Q, which is related to the wavelength of the incident radiation, λ and the scattering angle, θ by $Q = 4\pi \sin\theta/\lambda$. As such, the units of Q are inverse length and are normally reported for convenience in either nm^{-1} or Å^{-1}. A properly carried out experiment will yield $I(Q)$ in absolute intensity units, again an inverse length, which are conventionally reported in cm^{-1}. The measured $I(Q)$ includes both coherent and incoherent elastic scattering, with the coherent scattering providing the useful information on scattering structures. The incoherent scattered intensity is Q-independent and therefore manifests as flat background noise.

The main parameters affecting the coherent signal are the form (shape and size) of the structures giving rise to scattering, denoted as $P(Q)$, their number in a given volume and their 'contrast' with respect to the background medium. For ordered samples, charged particles or dispersions at high concentrations,
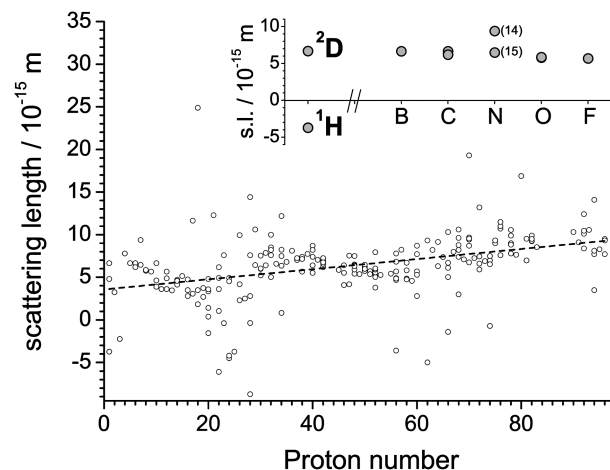

Fig. 1 Plot of coherent scattering length *vs.* proton number for all naturally abundant elemental isotopes up to curium. Values taken from ref. 18. (Inset) Plot of the coherent scattering lengths of some selected light elements.

scattering from the structure, $S(Q)$ is observed if it lies within the measured Q-range. The 'contrast' originates from the difference in scattering length density, $\Delta\rho$ between the scattering structures, $\rho_{\text{scatterer}}$ and the solvent medium, ρ_{solvent}. The values of ρ are a summation of the scattering lengths of the atomic components divided by the occupied volume. Therefore, they can be calculated from the empirical formula of a material, provided the density is known.[17] This raises a significant point, which is that ρ can be altered both by the atomic composition of a material and its density.

Neutrons scatter from interactions with sample nuclei. Unlike X-rays, the neutron scattering length of a given element is not strongly correlated with its proton number, but is isotope dependent. Fig. 1 shows a plot of the neutron (coherent) scattering length *versus* proton number for all elements up to curium.[18] As can be seen, most scattering lengths lie within the range of 1–11 × 10^{-15} m, with noticeable variations for isotopes of the same element. Inset on Fig. 1 is a plot focussing on some of the lighter elements, highlighting in particular the large difference in scattering length between ^{1}H and ^{2}D. Correspondingly, SANS is especially appropriate for the study of hydrogen-rich organic materials, in which isotopic labelling by selective deuteration, 'contrast variation'[19] can be used to highlight regions within a sample. Specific uses of this approach will be outlined in more detail in Section 2.1.

1.2 Data analysis

As already noted, SANS intensity, $I(Q)$ is related to the volume, shape, contrast and concentration (volume fraction) of the nano-scale structures present in a sample. The contributions to $I(Q)$ for a particle of specified shape and size is described by its form factor, $P(Q)$. A general rule is that small things scatter slightly at larger Q, whereas larger things scatter strongly at smaller Q. Because of this it can be quite easy to extract volume, V and volume fraction, ϕ information from SANS data, given a known particle shape and contrast. This is especially true for
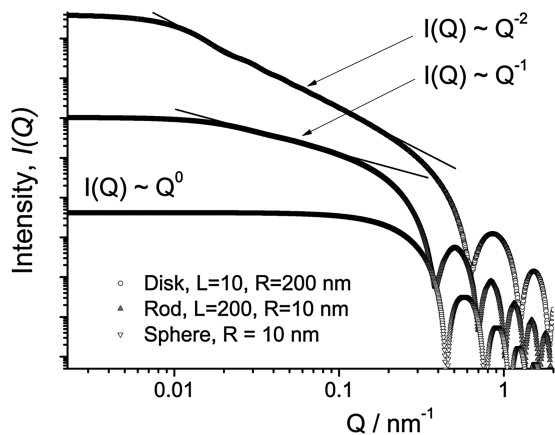
Fig. 2 Simulated ideal scattering from simple monodisperse particle shapes, calculated using the SASfit software.

relatively dilute, non-interacting systems, for which $I(Q)$ additionally tends to $V\phi(\Delta\rho)^2$ at low values of Q.[10,13,14]

Monodisperse particles of different simple shapes exhibit characteristically different scattering, as shown in Fig. 2. The $I(Q)$ for all shapes exhibits high Q oscillations, which decay in proportion to Q^{-4}. Additionally, the rods exhibit a region in which $I(Q)$ scales with Q^{-1}, which for disks is Q^{-2}, as indicated in Fig. 2. The spherical particles give rise to a large region (for $QR < 1.3$) in which $I(Q)$ appears to be independent of Q. This is actually present for all shapes for $QR_g < 1$, where R_g is the radius of gyration, and can be used to gain size information, using Guinier analysis.[9,10,13–16,20] For spherical scatterers, this involves plotting $\ln[I(Q)]$ *vs.* Q^2, where the gradient is equal to $(-R_g^2/3)$. Other simple plotting methods include the Porod plot ($\log_{10}[I(Q)]$ *vs.* $\log_{10}[Q]$) shown in Fig. 2, used to extract the fractal dimension of the scattering objects, and Zimm or Kratky plots, used to obtain information on the aggregation behaviour or chain confirmation of polymers in solution.[9,10,13–16,20] These treatments are useful to obtain first order approximations, but for a better understanding of all but the simplest systems, more complex analyses should be used. One method involves fitting the SANS data to a combination of theoretical models representing the shapes and size distributions of the scatterers within the sample. To do this, various software packages are available. These include standalone programs such as FISH by Heenan (ISIS),[21] SASfit by Kohlbrecher and Bressler (PSI) and the recently shipped SasView, developed through the work of several collaborators on the NSF DANSE project. Additionally, plugins (for Igor Pro) are available including the NCNR SANS package by Kline (NIST)[22] and IRENA by Ilavsky (ANL).[23] Typically, these programs come with detailed, fully referenced documentation, hundreds of customisable combinations of models and can be used with relative ease to obtain a variety of information about the investigated system. Several excellent guides to model fitting and data analysis exist, including "The SANS Toolbox", available from NIST.[20]

However, as with any complex fitting method, the reliability of the results is dictated by the number of prior known factors. This is particularly true when the shape is unknown and can be

further complicated by polydispersity, which tends to smear data features. Small-angle scattering data contains insufficient information[24] to separately determine shape and size distribution from a single dataset. For example, a polydisperse solution of relatively short rods can usually be equally well approximated by populations of polydisperse spheres or ellipsoids. Compounding this, higher concentrations typically bring about changes in the scattering due to $S(Q)$ and the formation of aggregates or fractal structures. These factors severely complicate data analysis and often necessitate approximation. As real systems typically involve poorly defined shapes, multiple approximated contrasts, higher concentrations or all of the above, accurate model fitting of their SANS can be difficult in the absence of other information. The presence of interparticle $S(Q)$ can be particularly difficult to deal with in non-spherical or polydisperse systems, although approximations do exist.[25–29]

The use of contrast variation and the application of the same analysis to multiple datasets can go some way to overcoming these issues, by reducing the number of possible explanations for a given dataset. Additionally, other 'form-free' ways to analyse SANS data are available, for example the Indirect Fourier Transform (IFT) by Glatter[30] or the numerical methods suggested by Magnani *et al.*[31] and recently Pauw *et al.*[32] These yield probability distributions of the length-scales of the scattering objects and can be powerful, 'assumption-free' ways to determine information on particle shapes and sizes. For example, as shown in Fig. 3, the shapes and dimensions of simple aggregate structures that form in solution can be easily elucidated by inspection of the IFT probability distribution.[33] However, for more complicated systems or those containing significant $S(Q)$, the generation and interpretation of the probability distributions is not straightforward. In these cases, assumptions (*e.g.* concerning shape) must usually be made in order to obtain physically relevant parameters to facilitate comparisons.

Taking all of this into account, SANS data from complicated systems should almost always be analysed alongside information derived from other techniques. With this information, it becomes much easier to justify a chosen model or interpret
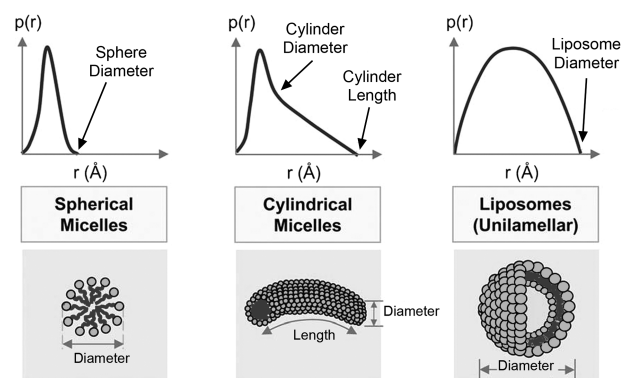

Fig. 3 Typical IFT results for simple self-assembled structures: spherical micelles, cylindrical micelles and liposomes (vesicles). Adapted from ref. 33 with permission from The Royal Society of Chemistry.

the size distributions generated by form-free methods. Doing this permits the strengths of SANS (or indeed any scattering technique) to be better exploited.

A final note on data analysis concerns error estimation. As noted elsewhere,[34] "a fitting procedure should provide (i) parameters, (ii) error estimates on the parameters, and (iii) a statistical measure of goodness-of-fit. When the third item suggests that the model is an unlikely match [poor fit] to the data, then items (i) and (ii) are probably worthless." As a rule, SANS facilities provide error estimates alongside Q and $I(Q)$ data columns. However, it is up to the users to measure for sufficient lengths of time, thereby minimizing the error on individual data points, which directly affects the error on fitted parameters. Data analysis must then be done carefully and should take goodness-of-fit values into account (e.g. reduced χ^2),[32] which most SANS fitting programs provide. This is particularly applicable to SANS on complicated systems for the afore-mentioned reasons.

2. Applications of SANS

2.1 Amphiphilic self-assembly

Self-assembled soft materials comprise nanoscale building blocks or domains that are normally within the size range detectable by SANS. In addition to those already mentioned above, several excellent reviews on data analysis specific to soft matter systems are available.[35,36] For self-assembling organic species in solution, SANS is particularly useful because of the afforded high contrast between a ^{1}H-rich material and a ^{2}D-rich solvent. Consequently, one of the more common uses of SANS is for the characterisation of aggregate structures of surfactants,[37–41] block copolymers[42,43] or asphaltenes[44,45] in deuterated solvents. Ternary systems such as emulsions,[46] microemulsions[47–51] and liposomes[33,52,53] are also investigated, for a variety of purposes including mustard gas decontamination,[50] art restoration,[51] and drug delivery.[33] In this case, selective deuteration of the different components is frequently used to obtain a more detailed structural picture, as highlighted in Fig. 4. The case of a microemulsion is shown, with a water droplet 'core' and surfactant 'shell', although the same principle can be applied to a wide variety of systems (e.g. nanoparticle dispersions[54]). The difference between the SANS profiles is clear throughout the Q-range. Simultaneous fitting gives far more information on the system than can be obtained from individual contrasts.[49] In the case of the core contrast, typically the surfactant and solvent are both deuterated. In addition to the coherent scattering of interest to SANS analysis, ^{1}H exhibits strong incoherent scattering which manifests as (flat) background noise, as noted above. This effect is particularly damaging at high Q, where $I(Q)$ is lower, and can drown out the coherent scattering signal. By minimizing the ^{1}H content, the signal resolution is therefore increased, permitting easier data analysis. This is especially important for SANS measurements of small spherical objects (e.g. microemulsion droplets with low water content), for which $I(Q)$ can be quite low.
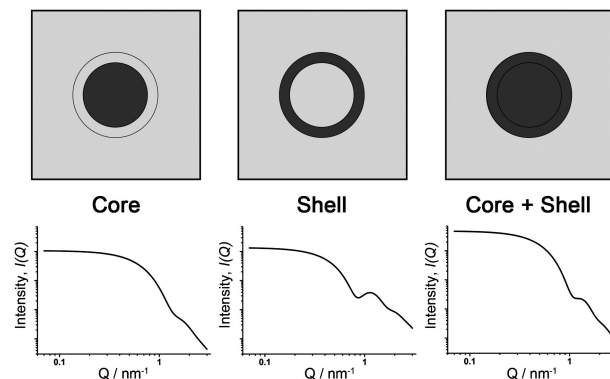

Fig. 4 An example of contrast variation SANS using solvent deuteration. In the schemes, the parts labelled with ^{2}D are represented by light grey, ^{1}H with dark grey. Simulated SANS is shown beneath each scheme for a typical Schultz-Zimm distribution of droplets with average core radii of 3 nm, shell thickness of 1 nm and variance, $\sigma = 0.2$.

Another way to generate additional contrast can be by comparing SANS results with those obtained from SAXS. Because of the different origins of scattering contrast (cf. scattering basics section), SAXS data arises mostly from electron dense parts of an assembly, while SANS will highlight the ^{1}H- or ^{2}D-rich regions. This approach is particularly appropriate for molecules containing both aromatic (e$^-$-rich, H-poor) and aliphatic (H-rich, e$^-$-poor) parts, such as asphaltenes[44,45] or fullerene derivatives,[55] but can be also used to locate nano-particles in biphasic systems.[56]

One particularly important application of SANS to self-assembled systems has been in identifying amphiphiles cap-able of modifying the properties of liquid and supercritical CO_2.[57–59] CO_2 is a green solvent with the potential to replace the volatile organic compounds currently used in industrial pro-cesses, but is poorly compatible with most materials.[60] Various approaches have been proposed to improve its solvency and otherwise influence its properties, including surfactant design[57,61,62] and solvent engineering.[63,64] Amphiphiles have been identified that can aggregate[65,66] and disperse water droplets[67–70] or nanoparticles[71–74] in liquid CO_2, or modify its viscosity.[75–77] High-pressure SANS (HP-SANS) has been used throughout to provide definitive evidence for the formation of the proposed structure and information on its length scale. The structures are measured in situ under pressurised conditions, hence HP-SANS. The contrast between CO_2 ($\rho \sim 2.5 \times 10^{10}$ cm^{-2}) and a typical hydrocarbon amphiphile ($\rho \sim 0.5 \times 10^{10}$ cm^{-2}) is sufficient, so a SANS signal in the detected Q-range (e.g. 0.01–0.3 Å^{-1}) is strong evidence for dispersions of nano-sized aggregates. This approach has been used to confirm the aggregation (or lack thereof) of both custom-designed surfactants in pure CO_2[65] and commercial surfactants in CO_2–alkane mixtures.[63] For microemulsion droplets in CO_2, both H_2O (-0.56×10^{10} cm^{-2}) and D_2O (99% D, 6.33×10^{10} cm^{-2}) droplets provide sufficient contrast, although to reduce the aforementioned flat background arising from ^{1}H content, D_2O is usually preferred. Both spherical and rod-like microemulsion droplets have been identified,[67–69,76,77] with

additional evidence for the latter provided by high-pressure viscosity measurements. Continued improvements in pressure-cell technology now permits the use of wider neutron beams and thicker cells, increasing the volume capable of being visualized and improving data resolution.[62,67]

2.2 Supramolecular self-assemblies

SANS has also been used to characterise supramolecular assemblies, including self-assembling supramolecular polymers,[78] oligoelectroytes[79] and fullerene derivatives.[55,80] In these cases, SANS was employed for its ability to directly detect assembly structures in solution, with information from spectroscopy, microscopy or SAXS used to back up the analysis. In supramolecular chemistry, the ability to measure solution assembly structures is important as they often differ wildly from the solid-state assemblies of the same material and can provide the seeds from which they form. However, due to multiple non-covalent forces directing self-assembly (e.g. hydrogen bonds, aromatic interactions, ionic attractions, donor–acceptor pairs etc.), a greater variation in shape can be expected than for the simpler amphiphilic systems described above. Because of this, structural characterisation by SANS is best carried out in combination with other techniques. In doing so, the error resulting from the aforementioned difficulty in separately determining shape and size distribution is reduced. For example, pyrogallol[4]arenes with added metals (M = Ni, Cu, Ga, Zn) or organic guests (e.g. pyrene) can self-assemble into dimeric or hexameric capsules or hollow cylinders/tubes.[81–83] In all cases, SANS was used alongside other techniques (e.g. XRD and NMR) to characterise assembly structures. However, for the capsules SANS was additionally used to elucidate the role of the reaction conditions on the ratio of the dimer and hexamer products.[81] Based on their structures determined by single-crystal XRD, dimers and hexamers were calculated to have radii of 7 and 10 Å respectively. Despite this similarity, the data were modelled using a bimodal distribution of spheres and the volume fraction of each population was extracted. As the structure, shape and size of the capsules were already known, the error in the determined volume fractions is reduced. From the resulting volume fractions it was inferred that the dimers are the more stable thermodynamic product, while the hexamers are a kinetic product that gradually convert to dimers over time.

2.3 P3HT-containing gels and films

A particularly interesting application of SANS to functional soft matter has been in systems containing poly(3-hexylthiophene), P3HT. This conjugated polymer is extensively studied for organic electronic devices due to its relatively high hole mobility and solution processability. Creating well-defined assemblies of P3HT on the nano- and mesoscale is important as the assembly properties directly affect device performance. P3HT is known to gel aromatic solvents on cooling from the fully dissolved solution state.[84–86] The gel structure was determined by microscopy (AFM, TEM) to consist of bundled fibres. However, as a 2D image of a 3D sample,[87] microscopy suffers an inability to reliably distinguish between overlapping fibres and

branched network. This is important as a network throughout which charge can freely move is expected to have better electrical properties (e.g. charge transport) than interdigitated fibres. In order to better characterise the system, both SANS and ultra-SANS (USANS)[11,12] were used. USANS equipment is currently less commonly available than SANS, but greatly increases the size of scattering objects that are able to be detected to over 10 μm. By combining the data from both techniques, it is possible to detect length scales in the sample from 1 to 10 000 nm. This permitted the visualisation of (i) the parallelepiped-shaped unit assemblies of P3HT molecules, (ii) the fibres consisting of multiple parallelepipeds, (iii) the network structure of the fibres and (iv) the extent of the networks on the same plot (Fig. 5).[84] The parallelepiped model was chosen to reflect the orthorhombic crystal structure of P3HT, although cylindrical models have also been used to fit SAXS data of similar systems.[88] The fractal dimension, D_f of the network[20,89] was obtained as the exponent of the power law scattering (blue line, Fig. 5). The length scale "d_{onset}" was defined as the point in Q at which the data deviates from being able to be explained using the parallelepiped model. This indicates the limit to which the scattering can be considered as arising from individual fibres – i.e. an approximate distance between branches or overlaps detected by SANS. Higher values of D_f and lower values of d_{onset} both indicate a denser network. D_f values ranging between 1.4 and 1.9 were almost always obtained,[84–86] indicating branched networks. Interestingly, while changing sample conditions led to some variations in the network density and its mechanical and electrical properties, little change in the scattering at higher Q was observed. This indicates that the underlying fibre structure was similar in all cases. As expected, higher conductivity was obtained by increasing branching within the networks.[85]

SANS has also been applied to films comprising P3HT and the fullerene derivative PCBM ([6,6]-phenyl-C_{61}-butyric acid methyl ester).[90] As one of the most studied organic p-type
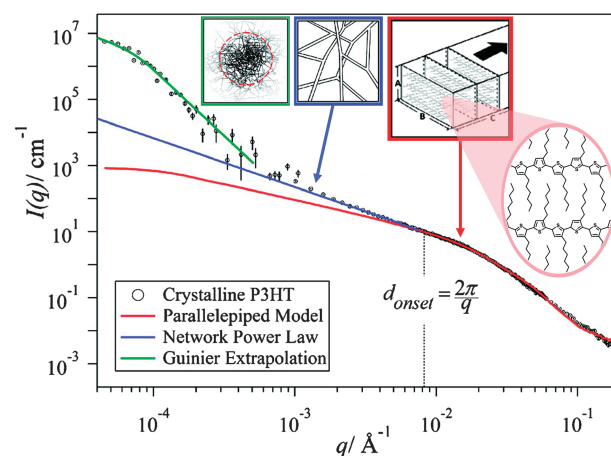

Fig. 5 Combined SANS and USANS data from 0.2 wt% P3HT in p-xylene. The data are fit using models (solid lines) that describe the structures at different length scales. The insets are schematic representations of the structural features characterized by the fitting. Adapted with permission from ref. 84. Copyright 2011 American Chemical Society.

and n-type semiconductor films for bulk heterojunction solar cells,[91] the ability to correlate their structure and efficiency is vitally important. Because of the difference in scattering length density, ρ between the carbon-rich PCBM (4.4×10^{10} cm^{-2}) and carbon and hydrogen containing P3HT (0.7×10^{10} cm^{-2}, *cf.* Fig. 1, inset), the contrast is high without the need for deuteration. Detailed SANS experiments have been carried out to investigate the effect of composition and thermal or solvent annealing processes on film structure.[92,93] For all compositions (10–50 vol% PCBM), SANS profiles with scattering peaks corresponding to crystalline P3HT were noted. However, only the 50% PCBM sample exhibited a noticeable peak corresponding to crystalline PCBM. Additionally, a much larger $I(Q)$ at low Q was noted than for the other samples. Both of these factors point to P3HT and PCBM crystals being phase separated. The remaining SANS was explained as arising from P3HT crystals. These were modelled as prolate ellipsoids with lengths of 25–30 nm, whose size were relatively independent of concentration. From this analysis a detailed structural picture of the films was proposed, consisting of PCBM and P3HT crystals separated by a miscible phase of amorphous P3HT:PCBM (Fig. 6).[92] This result is in line with the high miscibility of PCBM and P3HT[94,95] and would be very difficult to obtain using a technique other than SANS.

For the 1:1 P3HT:PCBM films, data analysis of the (high Q) Porod regime suggested interfacial mixing with increased thermal annealing time. In this region, which contains information on interfacial roughness, $I(Q)$ scales in proportion to Q^{-a}. For rough interfaces, a ranges from 3 to 4, with a value closer to 4 (the theoretical value for a sharp interface) indicating an increased sharpness. For the films, the interfacial roughness can be equated with interdigitation between P3HT and PCBM phases. At longer annealing times, the value of a decreased, implying increased interfacial mixing. Several other groups have noticed similar effects.[94,96]

On the other hand solvent annealing,[93] which is a more practical way to form films, was found by SANS to lead to initial intermixing,
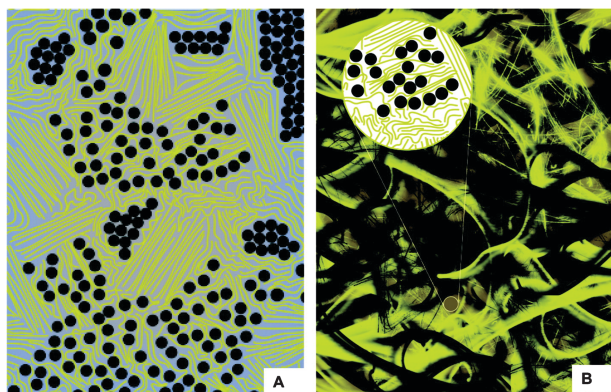
followed by phase separation of PCBM that is driven its solubility limit (around 22%)[95] in amorphous P3HT. These changes were correlated to photovoltaic activity, which significantly improved after solvent annealing, indicating the formation of crystalline PCBM within the film to be crucial to device efficiency.

An important point about the two examples above (P3HT gels, P3HT:PCBM films) is that they both concern relatively complex systems. Despite this, the structure has been thoroughly characterised, using a combination of direct SANS profile interpretation (*e.g.* identifying power laws) and careful modelling of the data. In doing so, links between the internal structure (over a range of length scales) and the bulk properties have been identified, which would have been difficult or even impossible to establish using other techniques.

2.4 Mixing and alignment

The applications of SANS to polymerisable surfactants,[97] polymer colloids[5] and hydrogels[7,98] have all been reviewed very recently. In general, SANS has been used for structural characterisation of these materials, with similar data treatments to those outlined above. Elsewhere, SANS has been used to accurately characterise the nanoscale mixing of soft solids, represented by micelles of poly(styrene-*block*-ethylene-*alt*-propylene), PS-PEP.[99] With any other technique, such direct verification of homogenization would be very difficult, but using contrast variation SANS it was possible. Solutions of PS(^{1}H)-PEP and PS(^{2}D)-PEP in squalene (42 vol% $C_{30}H_{62}$ and 58 vol% $C_{30}D_{62}$) were mixed and measured by SANS. This mixture of ^{1}H- and ^{2}D-squalene was chosen so that contributions to the SANS from the $S(Q)$ would be eliminated on complete mixing, as was observed to occur. The $S(Q)$ was still present in separate SAXS results taken after blending, indicating that the only change was mixing between ^{1}H- and ^{2}D-micelles.

SANS can also be used to study aligned systems. For example, liquid crystalline mesophases,[100–102] colloidal crystals[103] and opals[104] have been investigated. In all cases, SANS can be used to both detect and quantify alignment. To do this, the two-dimensional detector image is used, prior to radial integration to obtain $I(Q)$ *vs.* Q. Alignment causes the detector pattern to become markedly anisotropic (*cf.* Fig. 7). Performing an azimuthal (constant Q) scan gives a plot of scattered intensity *versus* annular angle, from which an order parameter, representing the extent of alignment, can be calculated.[100–102,105] Alignment can be achieved by several methods, including nanoscale confinement within a porous template[100] or the direct use of an externally magnetic field, coupled with sample rotation.[101] Another method involves the confinement of magnetite nanoparticles within the grain boundaries of the hosting mesophases.[102] On application of an external magnetic field, the nanoparticles align, which in turn aligns the mesophases, shown in Fig. 7 for a hexagonal phase. Significantly, this neat approach can align mesophases containing molecules that are not strongly affected by the applied field.
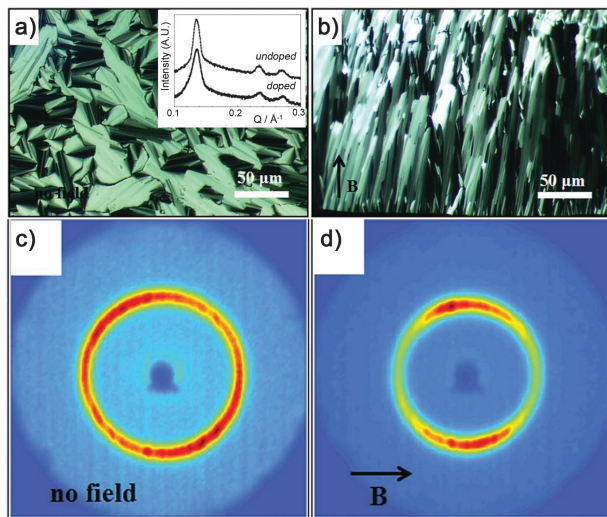

Fig. 6 Diagram showing the ''rivers and streams'' model for P3HT:PCBM films proposed by SANS. In both images, yellow incidicates P3HT and black indicates PCBM. Crystals are implied by ordering of the lines and circles. In (B), brown regions indicate amorphous P3HT + PCBM. Reprinted with permission from ref. 92. Copyright 2011 American Chemical Society.

Fig. 7 (a, c) Polarising optical microscopy, POM and SANS detector images of disordered hexagonal phase containing magnetic particles. (inset, a) SAXS data for doped and undoped systems, showing minimal changes with particle incorporation. (b, d) POM image and SANS detector images of the same system after the application of a magnetic field to induced alignment. Adapted from ref. 102 with permission from The Royal Society of Chemistry.

Finally, SANS has been employed to measure the flow of hydrogels, polymer melts, clays, emulsions, micelles, membrane phases and biological systems. For more detail, readers are pointed to a recent comprehensive review of this area.[6]

2.5 Carbon dispersions

Allotropes of carbon, especially nanotubes (CNTs) and graphene are of significant interest for their wide range of impressive properties. The ability to purify and process these materials into desirable structures or assemblies is fundamental to many potential uses and is strongly facilitated by their ability to be dispersed in solvents. Efforts to improve solubility have included chemical functionalisation or the addition of amphiphiles such as surfactants or block copolymers. It is particularly important to measure the extent of debundling (nanotubes) or delamination (graphene), as this will be related to the quality of the final desired material. SANS is a useful technique for doing this, as it can provide information both on the dispersion quality and on the surrounding additives[106] or grafted chains.[107] In the case of CNTs, the expected SANS data for an unbundled dispersion should theoretically contain a wide region in which $I(Q)$ scales in proportion with Q^{-1}, characteristic of a dispersion of long rod-like particles (*e.g.* Fig. 2). However, such a perfect dispersion is found only rarely under dilute conditions, with a large quantity of dispersant.[108] Example data is shown in Fig. 8,[109] alongside a schematic depiction of the structures detected. In the low Q region, $I(Q)$ is typically found to scale in proportion with Q^{-a}, with a lying between 2 and 3,[106–111] indicative of a dense fractal network similar to those discussed for the P3HT gels. As before, a decreased value for the exponent indicates a less dense network, which is also reflected in the onset point of the fractal structure (approx. 0.06 $Å^{-1}$ in Fig. 8). The behaviour in the high
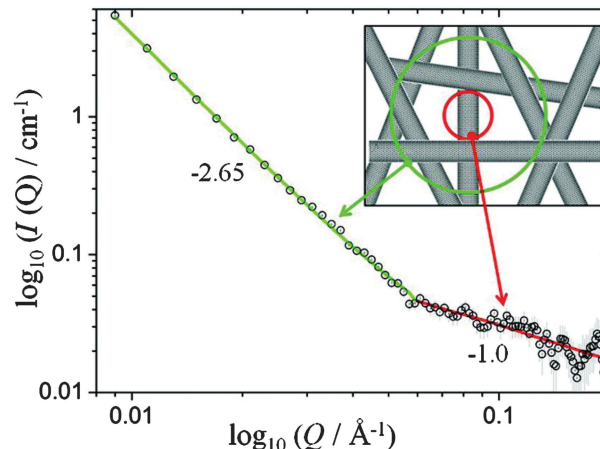

Fig. 8 Example SANS from a network of unbundled carbon nanotubes, and (inset) a schematic description of the data. Reprinted with permission from ref. 109. Copyright 2012 American Chemical Society.

Q region gives information on the state of the individual tubes. As CNTs are rods, data analysis in this region is typically carried out using cylindrical models.[106,107,109] In the case shown in Fig. 8, the slope in the high Q of 1.0 disappearing into the background strongly indicates extensive unbundling of the tubes.

Recently, the same approach was applied to dispersions of graphene.[112] The layers were intercalated with potassium–ammonia solution and then dissolved in THF to yield a suspension of negatively charged graphene platelets that was characterised by SANS. As noted in Fig. 2, dispersed platelets (disks) are expected to exhibit a region in which $I(Q)$ scales with Q^{-2}. This was observed, but the onset point of the region appeared at quite low Q (around 0.02 $Å^{-1}$) and may therefore arise from platelet stacks. Model fitting was employed, using a relatively complicated model including contributions from both platelet stacks and completely exfoliated platelets, the evidence for which was derived from AFM measurements on drop-cast films on mica. The results from data analysis indicated fully separated platelets to be present in solution, although at a relatively low level as a fraction of the total volume of dispersed graphene. Given that the platelet size observed by AFM was 100–250 nm, the radius of graphene platelets detected by SANS (15 nm) was thought to indicate the extent over which the flexible graphene sheets can be considered to be rigid.

2.6 Porous materials

SANS perceives dense networks surrounded by a less dense medium (as in the above examples) in much the same way as a dense medium containing a less dense network of pores. Examples of the types of structures that can be analysed are given in Fig. 9, alongside example SANS data for activated carbon.[113] SANS from porous structures is typically characterised by (i) power-law dependent scattering (blue region in Fig. 9d), combined with (ii) a form factor for the pore shape and size (yellow region in Fig. 9d). This makes it possible to obtain
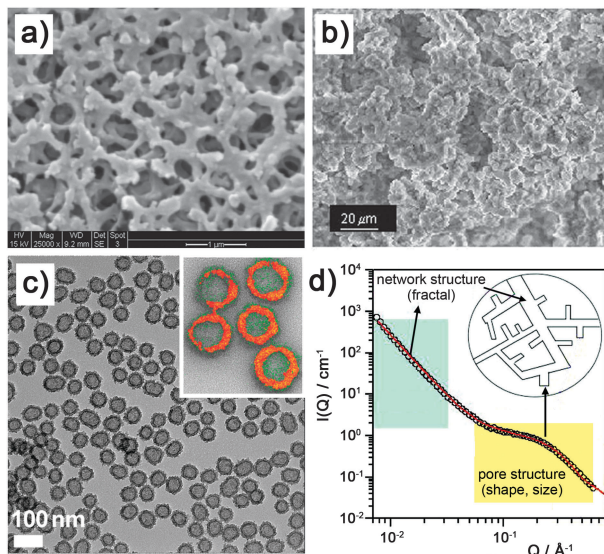
Fig. 9 Examples of porous media that have been studied by SANS: (a) SEM image of a Millipore mixed cellulose ester membrane, reprinted from ref. 114, with permission from Elsevier. (b) SEM image poly(4-vinyaniline)/polydivinylbenzene monolith, reprinted with permission from ref. 115. Copyright 2011 American Chemical Society. (c) TEM image hollow silica/titania nanoparticles. (Inset, c) EELS dot mapping of five nanoparticles; false color code: Si = green, Ti = red. Reprinted with permission from ref. 120. Copyright 2012 American Chemical Society. (d) Example SANS data for porous activated carbon, highlighting the contributions from the network and average pore structure to the overall scattering (shaded regions, as labelled). Reprinted with permission from ref. 113. Copyright 2010 American Chemical Society.

pore size distributions alongside information on the density and structure of the porous networks. For samples containing a large single pore size or multiple pore-size distributions, USANS is often used.[114–117] Additionally, measurements combining SAXS and SANS,[114,118] or using contrast variation SANS, with either [1]H- or [2]D-toluene contained within the pores,[119] can be used to gain more information and highlight particular regions within a structure. SANS has also recently been employed alongside a variety of other techniques (*cf.* Fig. 9c) to study the structure and porosity of hollow silica/titania particles.[120] Ref. 115 provides a useful tabular summary of the range of porous structures that have been studied using small-angle scattering.

In addition to characterising pore structure, the functionalization of MCM41[118] and the ability of porous carbon to adsorb hydrogen has been investigated.[113,121] In this latter case, the specific benefits of SANS were an ability to characterise the preferential uptake of hydrogen into different pore sizes at different pressures and to evaluate its density within pores.[121] These latter studies are important due to the need for media capable of storing hydrogen for future transportation applications.

2.7 Precipitates and clusters

A final common application of SANS is to characterise the internal structures of hard materials such as silicate glasses,[122] zirconium-based alloys[123] and steels.[124] In steels and other alloys, treatments such as ball-milling,[124] tempering[125] and

thermal annealing[123,124] typically induce the formation of nano-scale precipitates, which can have profound effects on the material properties. The ability to characterise these particles is meaningful in order to establish structure–property relationships. SANS is particularly valuable for its ability to measure fairly thick samples *in situ* (*i.e.* with no complicated preparation methods) and to give statistical meaningful data on particulate size and volume fraction. Other benefits of SANS again include the ability to use complex sample environments, for example to measure samples under applied load.[126]

In addition to SANS deriving from interactions of the neutron beam with the nuclei within a material, neutrons also scatter from atomic magnetic moments. This is not so important for the examples described in the previous sections, but is clearly important when using SANS to characterise steels. If an external magnetic field is applied, the magnetic neutron scattering[127] is most pronounced perpendicular to the field and tends to zero in the parallel direction.[125] This can provide a way to remove the additional SANS arising from magnetic scattering,[128] but can also be used to select data arising from just the magnetic structure. To do this, measurements of the detected scattering in both positions are subtracted from one other to give the SANS from magnetic scattering alone.[125,129] This allows contributions from magnetic nanostructures within a sample (or nonmagnetic particulates within steel) to the overall SANS to be separated. The ability to do this is particularly powerful in the study of superconducting materials, as it permits the bulk flux line lattice structure to be measured.[130,131] At present, SANS remains unmatched in its ability to do this.[132]

Example magnetic scattering data for a sample of tool steel is shown in Fig. 10, which indicates a broad spectrum of particle sizes. In this case, the scattering is assumed to arise from non-magnetic particulates within the ferromagnetic medium. The data were modelled using four Gaussian distributions of spherical particles, which were assigned as carbon clusters (D1) and various metal carbides (D2–4) using microscopy and atom probe measurements. The change in the populations was observed with increased tempering time and was found to agree well with simulated behaviour.[125]

Another way to gain more information on the precipitates in steels and other alloys is by the use of combined SAXS and SANS measurements. Individually, these techniques can provide size distributions and volume fractions, allowing for cross-referencing. However, using a method denoted as 'alloy contrast variation' (ACV)[133] the chemical composition of the precipitates present in the sample can also be determined. This is because their volume fraction, size distribution and form are the same for both SAXS and SANS. Only the contrast differs and by splitting the data into regions corresponding to each particle size distribution and calculating a relative intensity, a ratio specific to the particle composition and crystal structure is obtained. This can be compared to the values calculated for expected precipitates. Systems studied using the ACV method include oxide clusters,[133] sulfide inclusions[134] and carbide precipitates[128] in a variety of different steels. This attractive method has advantages over TEM and even atom probe analysis,
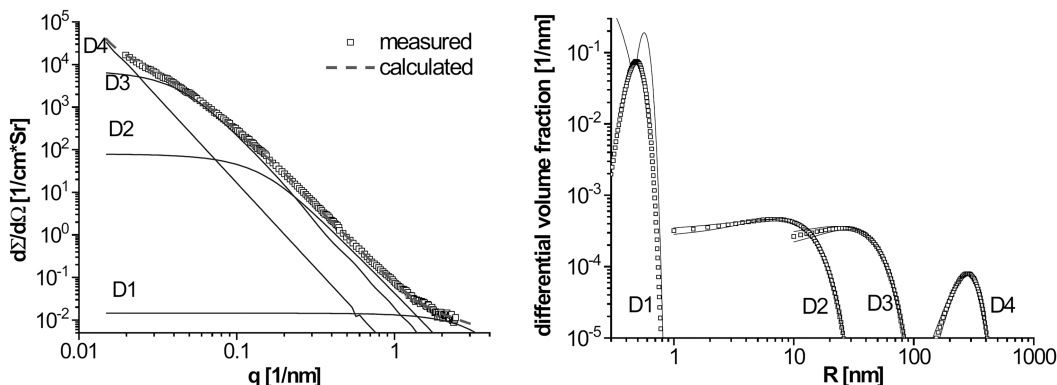
Fig. 10 (a) Magnetic neutron scattering data for as-quenched tool steel. Lines represent the scattering from four Gaussian particle distributions D1–4. (b) Fitted particle size distributions D1–4, with error indicated by thin grey lines. Reprinted with permission from ref. 125. Copyright 2006 J. Wiley and Sons.

mainly in that it requires no sample perturbation, and could clearly be applied to other systems to gain insights into composition and crystallinity.

3. Time-resolved SANS (TR-SANS)

Due to a continued improvement in beam line technology, SANS studies with time resolution less than 100 ms are now becoming routine. TR-SANS has been applied to a wide range of systems,[4,135,136] a few of which will be described here. The first of these is the observation of morphological changes within self-assembling systems that occur on mixing. This includes the formation of a microemulsion from a lamellar phase comprising surfactant and water on toluene addition[137] and the formation of liposomes from mixed surfactant solutions (Fig. 11).[138] Both of these processes have been carried out using the stopped-flow cell available at the ILL.[4] Given the ability to thoroughly characterise their underlying structures using SANS (see above), the application of TR-SANS to such systems is clearly appropriate. However, as these transitions occur quickly, short time frames for data collection are necessary, with a minimum of 20 ms. To collect statistically significant data suitable for analysis, each process is typically repeated several times and the intensities averaged. Fig. 11a shows TR-SANS data for the transition from a lamellar phase to a micro-emulsion.[137] Scattering from a lamellar phase is typified by a peak in the SANS representing the interlayer spacing (around $Q = 0.14$ Å^{-1} in Fig. 11a). Immediately after mixing (within 120 ms), the interlamellar spacing increased, in line with the formation of a solvent-swelled structure. After this, the change in model fitting parameters suggested a slow relaxation of the lamellar membrane to form the microemulsion (broad peak centred on 0.10 Å^{-1}). The timescales for the two steps were justified by the difference in energy required to swell the lamellar structure (low) *versus* that required to overcome the energy barrier of breaking up the lamellar membrane to form microemulsion droplets (high).

Fig. 11b shows snapshots of TR-SANS data taken during the formation of vesicles on mixing a zwitterionic surfactant, tetradecyl dimethyl amine oxide (TDMAO) and an anionic surfactant,
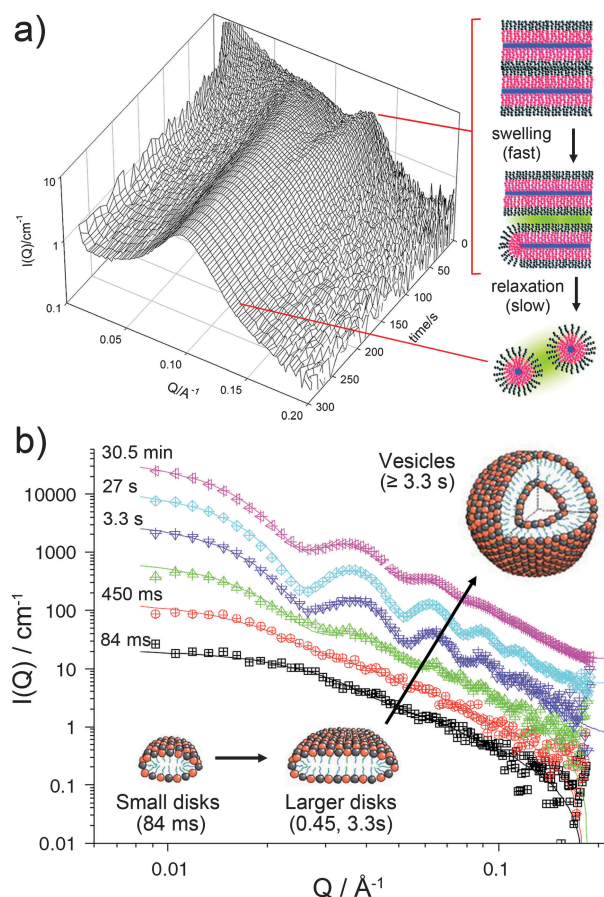

Fig. 11 (a) Time-resolved SANS data showing a lamellar to microemulsion phase transition triggered by toluene addition, with the two transition steps depicted schematically. Adapted from ref. 137 with permission from The Royal Society of Chemistry. (b) SANS data for a mixed sample of TDMAO (27.5 mM) and LiPFOS (22.5 mM) in D$_2$O for various times after mixing in a stopped-flow device, with cartoons schematically representing the species present in solution. The absolute intensity is correct for the 84 ms measurement. Subsequent curves were successively multiplied by a factor 3 for clarity. Solid lines are fits to the data. Adapted from ref. 8 and 139 with permission from The European Physical Journal (Springer) and The Royal Society of Chemistry.

lithium perfluorooctanesulfonate (LiPFOS).[8,138,139] Immediately after mixing, disk-like mixed micelles are formed, evidenced by

Perspective   PCCP

the region ($0.02 < Q < 0.1$ Å^{-1}) in which $I(Q)$ scales with Q^{-2}. As depicted, these quickly grow in size and within a few seconds close to form vesicles, as evidenced by the appearance of oscillations in the SANS. During this transition phase, represented by green and blue data points on Fig. 11b, both vesicles and disk-like micelles are thought to coexist in solution.

The ability to measure such structural changes in soft matter systems was recently applied to 1,2-dipalmitoyl-*sn-glycero*-3-phosphocholine (DPPC) liposomes.[140] The addition of phospholipase A2 (PLA$_2$) triggers a controlled release from within the liposome shell. The release is thought to proceed by initial shrinking of the liposomes, followed by their expansion and an increased shell permeability. To check this, the effect of adding PLA$_2$ to a solution of DPPC liposomes was tracked by TR-SANS over 12 h. As expected, SANS intensity initially decreased, due to liposome shrinkage from approximately 800 to 700 Å. This was followed (after around 4 h) by an increase in size to around 950 Å. The permeability of the membrane was also noted to increase, in line with the suggested mechanism.

TR-SANS has also been applied to the nucleation and growth of inorganic media.[136] For example, the protein-mediated nucleation and growth of CaCO$_3$,[141] the precipitation in Fe–Cu and Fe–Cu–B–N alloys[142] and the growth of nanocrystals in glass-ceramics[143] have all been investigated. A particular benefit of TR-SANS is the ability to separately visualize the organic template and the forming structure, both of which have a vital role in the growth mechanism. This was exploited recently in studies on the formation of mesoporous silica nanoparticles, MSNs in a solution of CTAB micelles.[54] Three different contrasted systems were used, designed to separately highlight (i) the silica MSNs, (ii) the micelles and (iii) both together. The reaction mechanism determined by modelling the TR-SANS data is shown in Fig. 12. After hydrolysis, initial condensation led to silica oligomers adsorbing to the micelle surfaces. This manifested in the SANS as a detected reduction in intermicellar repulsion, which drove the clustering of silica coated micelles to form larger micelle aggregates. Silica growth then took place around these structures. The remaining micelles not involved in these structures reduced in population and size throughout the reaction, with the latter effect thought to be due to methanol released during the hydrolysis of the

silica precursor. The effects of temperature and reagent concentration were also studied. In all cases, the reaction was observed to reach completion within 900 s, with an increased rate at higher concentrations. The final MSN sizes were corroborated by results from DLS, TEM and SAXS.

Finally, TR-SANS has been applied to observe structural changes during miniemulsion polymerisation[144] and a living radical polymerization to form a microgel-core star polymer.[145] Again, the application of TR-SANS is appropriate given the wealth of knowledge on the modelling of SANS data from polymer solutions.[35] For the formation of microgel-core star polymers, two stages were followed: (a) the process to form the poly(methyl methacrylate), PMMA arms and (b) their linking to form stars. Other *ex situ* techniques (NMR and size exclusion chromatography with and without multiangle laser light scattering) were used to back up the SANS analysis. In process (a), increases in $I(Q)$ were observed throughout the reaction, which were determined to be indicative of the growth of PMMA chains. Process (b) was determined to proceed in three stages. An initial increase in $I(Q)$ at low Q indicated the further growth of PMMA chains and their linking to form small star polymers. After this, an $S(Q)$ peak in the mid-Q range appeared, indicating a rapid increase in the number of star polymers in the solution and their corresponding increase in proximity. Finally, a subsequently slower increase in $I(Q)$ was noted, in line with the slow growth of a the microgel core.

A final point is that in all the above examples, the experiments have been optimised by using well-defined systems, averaging multiple runs to reduce data error, using contrast variation and/or including information obtained by other techniques. This is of particular importance for TR-SANS due to the necessarily shorter data collection times when studying fast processes.

4. Conclusions

It is hoped that this review has demonstrated the wealth of ways in which SANS can be exploited for the characterisation of materials systems. In particular, the use of contrast matching[5,19,42,49,99,119] or magnetic scattering[125,127,129,132] has been shown to be a valuable way to optimise experiments by highlighting structures of interest. Throughout the described examples, high importance is placed on the application of SANS alongside other scattering techniques. This can be used to increase the range of sizes detected, using USANS,[11,12,84,115] or to provide a different contrast, using SAXS,[44,45,55,56,114,118] from which material composition can additionally be estimated using ACV.[133] Additionally, the importance of evidence from microscopy techniques cannot be ignored as this provides critical information that can be fed into the SANS data modelling to increase accuracy.[78,79,81–84,100–102,112,114,115,120,125] In the condensed phase, the combination of multiple techniques can be used to build up detailed pictures, such as those established for P3HT gels and films.[84–86,92–95] The ability to generate such detail is clearly of benefit to the identification of structure–property relationships and SANS has a crucial role to play,
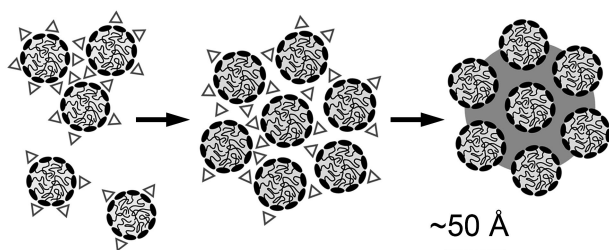

Fig. 12 Proposed growth scheme for the MSNs determined by TR-SANS. Micelles are represented by spheres, silica oligomers by triangles and condensed silica by grey shading. Reprinted with permission from ref. 54. Copyright 2012 American Chemical Society.

~50 Å

particularly in determining the statistically significant structural parameters. For soft dispersed media, the ability to measure the structure of solutions *in situ*, even in pressurized solvents[63,65–70,75–77] is of great advantage. Finally, using TR-SANS[4,135,136] changes within solutions or materials that occur on the ~100 ms timescale can be observed, permitting the structural study of nucleation and growth mechanisms,[54,136,141–143] polymerisation reactions[144,145] and other structural transitions.[137,138,140] The ability to do this in real-time *in situ* is almost exclusive to small-angle scattering techniques, with SANS of particular benefit in studying the growth of materials around an organic template.[54] Given the number of materials for which this true, SANS could yet become a key technique for mechanism elucidation in materials science.

Acknowledgements

Notes and references

1 Y. B. Melnichenko and G. D. Wignall, *J. Appl. Phys.*, 2007, **102**, 021101–021124.
2 M. Engel, T. Spehr and B. Stühn, in *Methods in Physical Chemistry*, ed. R. Schäfer and P. C. Schmidt, Wiley-VCH Verlag GmbH & Co. KGaA, 2012, pp. 297–324.
3 P. Fratzl, *J. Appl. Crystallogr.*, 2003, **36**, 397–404.
4 I. Grillo, *Curr. Opin. Colloid Interface Sci.*, 2009, **14**, 402–408.
5 M. Ballauff, *Adv. Eng. Mater.*, 2011, **13**, 793–802.
6 A. P. R. Eberle and L. Porcar, *Curr. Opin. Colloid Interface Sci.*, 2012, **17**, 33–43.
7 M. Shibayama, *Soft Matter*, 2012, **8**, 8030–8038.
8 M. Gradzielski, *Eur. Phys. J.: Spec. Top.*, 2012, **213**, 267–290.
9 O. Glatter and O. Kratky, *Small Angle X-ray Scattering*, Academic Press, London, 1982.
10 L. A. Feigin and D. I. Svergun, *Structure Analysis by Small-Angle X-Ray and Neutron Scattering*, Plenum Press, New York, 1987.
11 D. W. Schaefer and M. M. Agamalian, *Curr. Opin. Solid State Mater. Sci.*, 2004, **8**, 39–47.
12 M. A. Sharp, P. K. Pranzas and A. Schreyer, *Adv. Eng. Mater.*, 2009, **11**, 441–445.
13 R. M. Richardson, in *Colloid Science: Principles, Methods and Applications*, Blackwell Publishing Ltd, Oxford, 2005, pp. 228–254.
14 G. L. Squires, *Introduction to the theory of thermal neutron scattering*, Dover Publications, Inc., Mineola, NY, 1996.
15 R. Pynn, *Los Alamos Sci.*, 1990, **19**, 1–31.
16 A. J. Jackson, *Introduction to Small-Angle Neutron Scattering and Neutron Refrectometry*, NIST Center for Neutron Research, Gaithersburg, MD, 2008.
17 http://www.ncnr.nist.gov/resources/sldcalc.html.
18 V. F. Sears, *Neutron News*, 1992, **3**, 26–37.
19 H. B. Stuhrmann, *J. Phys.: Conf. Ser.*, 2012, **351**, 012002.
20 http://www.ncnr.nist.gov/staff/hammouda/the_SANS_toolbox.pdf.
21 R. K. Heenan, *FISH Data Analysis Program*, RAL-89-129, Didcot, UK, 1989.
22 S. R. Kline, *J. Appl. Crystallogr.*, 2006, **39**, 895–900.
23 J. Ilavsky and P. R. Jemian, *J. Appl. Crystallogr.*, 2009, **42**, 347–353.
24 C. G. Shull and L. C. Roess, *J. Appl. Phys.*, 1947, **18**, 295–307.
25 J. S. Pedersen, *J. Appl. Crystallogr.*, 1994, **27**, 595–608.
26 M. Kotlarchyk and S.-H. Chen, *J. Chem. Phys.*, 1983, **79**, 2461–2469.
27 D. Gazzillo, A. Giacometti, R. G. D. Valle, E. Venuti and F. Carsughi, *J. Chem. Phys.*, 1999, **111**, 7636–7645.
28 B. Weyerich, J. Brunner-Popela and O. Glatter, *J. Appl. Crystallogr.*, 1999, **32**, 197–209.
29 S. Hansen, *J. Appl. Crystallogr.*, 2008, **41**, 436–445.
30 O. Glatter, *Acta Phys. Austriaca*, 1977, **47**, 83.
31 M. Magnani, P. Puliti and M. Stefanon, *Nucl. Instrum. Methods Phys. Res., Sect. A*, 1988, **271**, 611–616.
32 B. R. Pauw, J.-S. Pedersen, S. Tardif, M. Takata and B. B. Iversen, *J. Appl. Crystallogr.*, 2013, **46**, 365–371.
33 O. A. Ogunsola, M. E. Kraeling, S. Zhong, D. J. Pochan, R. L. Bronaugh and S. R. Raghavan, *Soft Matter*, 2012, **8**, 10226–10232.
34 W. H. Press, S. A. Teutolsky, W. T. Vetterling and B. P. Flannery, *Numerical Recipes in C; The Art of Scientific Computing*, Cambridge University Press, New York, 2nd edn, 1992.
35 J. S. Pedersen, *Adv. Colloid Interface Sci.*, 1997, **70**, 171–210.
36 V. Castelletto and I. W. Hamley, *Curr. Opin. Colloid Interface Sci.*, 2002, **7**, 167–172.
37 M. J. Hollamby, R. Tabor, K. J. Mutch, K. Trickett, J. Eastoe, R. K. Heenan and I. Grillo, *Langmuir*, 2008, **24**, 12235–12240.
38 N. Baccile, F. Babonneau, J. Jestin, G. Pehau-Arnaudet and I. Van Bogaert, *ACS Nano*, 2012, **6**, 4763–4776.
39 M. Kotlarchyk, J. S. Huang and S. H. Chen, *J. Phys. Chem.*, 1985, **89**, 4382–4386.
40 A. M. Ketner, R. Kumar, T. S. Davies, P. W. Elder and S. R. Raghavan, *J. Am. Chem. Soc.*, 2007, **129**, 1553–1559.
41 H. Takeno, A. Maehara, D. Yamaguchi and S. Koizumi, *J. Phys. Chem. B*, 2012, **116**, 7739–7745.
42 J. S. Pedersen, I. W. Hamley, C. Y. Ryu and T. P. Lodge, *Macromolecules*, 2000, **33**, 542–550.
43 L. Yang, P. Alexandridis, D. C. Steytler, M. J. Kositza and J. F. Holzwarth, *Langmuir*, 2000, **16**, 8555–8561.
44 J. Eyssautier, P. Levitz, D. Espinat, J. Jestin, J. Gummel, I. Grillo and L. Barré, *J. Phys. Chem. B*, 2011, **115**, 6827–6837.
45 O. C. Mullins, H. Sabbah, J. Eyssautier, A. E. Pomerantz, L. Barré, A. B. Andrews, Y. Ruiz-Morales, F. Mostowfi, R. McFarlane, L. Goual, R. Lepkowicz, T. Cooper, J. Orbulescu, R. M. Leblanc, J. Edwards and R. N. Zare, *Energy Fuels*, 2012, **26**, 3986–4003.

46 G. Alvarez, J. Jestin, J. F. Argillier and D. Langevin, *Langmuir*, 2009, **25**, 3985–3990.

47 M. J. Hollamby, J. Eastoe, K. J. Mutch, S. Rogers and R. K. Heenan, *Soft Matter*, 2010, **6**, 971–976.

48 M. Kotlarchyk, S.-H. Chen, J. S. Huang and M. W. Kim, *Phys. Rev. A: At., Mol., Opt. Phys.*, 1984, **29**, 2054–2069.

49 S. Nave, J. Eastoe, R. K. Heenan, D. C. Steytler and I. Grillo, *Langmuir*, 2000, **16**, 8741–8748.

50 I. A. Fallis, P. C. Griffiths, T. Cosgrove, C. A. Dreiss, N. Govan, R. K. Heenan, I. Holden, R. L. Jenkins, S. J. Mitchell, S. Notman, J. A. Platts, J. Riches and T. Tatchell, *J. Am. Chem. Soc.*, 2009, **131**, 9746–9755.

51 M. Baglioni, D. Berti, J. Teixeira, R. Giorgi and P. Baglioni, *Langmuir*, 2012, **28**, 15193–15202.

52 S.-H. Tung, H.-Y. Lee and S. R. Raghavan, *J. Am. Chem. Soc.*, 2008, **130**, 8813–8817.

53 H. D. Andersen, C. Wang, L. Arleth, G. H. Peters and P. Westh, *Proc. Natl. Acad. Sci. U. S. A.*, 2011, **108**, 1874–1878.

54 M. J. Hollamby, D. Borisova, P. Brown, J. Eastoe, I. Grillo and D. Shchukin, *Langmuir*, 2012, **28**, 4425–4433.

55 U. Jeng, T.-L. Lin, W.-J. Liu, C.-S. Tsao, T. Canteenwala, L. Y. Chiang, L. P. Sung and C. C. Han, *Physica A*, 2002, **304**, 191–201.

56 M. J. Hollamby, J. Eastoe, A. Chemelli, O. Glatter, S. Rogers, R. K. Heenan and I. Grillo, *Langmuir*, 2010, **26**, 6989–6994.

57 J. Eastoe, S. Gold and D. C. Steytler, *Langmuir*, 2006, **22**, 9832–9842.

58 J. Eastoe and S. Gold, *Phys. Chem. Chem. Phys.*, 2005, **7**, 1352–1362.

59 J. M. DeSimone and J. S. Keiper, *Curr. Opin. Solid State Mater. Sci.*, 2001, **5**, 333–341.

60 W. Leitner, *Nature*, 2000, **405**, 129–130.

61 M. T. Stone, P. G. Smith, S. R. P. da Rocha, P. J. Rossky and K. P. Johnston, *J. Phys. Chem. B*, 2004, **108**, 1962–1966.

62 A. Mohamed, M. Sagisaka, M. Hollamby, S. E. Rogers, R. K. Heenan, R. Dyer and J. Eastoe, *Langmuir*, 2012, **28**, 6299–6306.

63 M. J. Hollamby, K. Trickett, A. Mohamed, J. Eastoe, S. E. Rogers and R. K. Heenan, *Langmuir*, 2009, **25**, 12909–12913.

64 J. M. Dobbs, J. M. Wong and K. P. Johnston, *J. Chem. Eng. Data*, 1986, **31**, 303–308.

65 J. Eastoe, A. Paul, S. Nave, D. C. Steytler, B. H. Robinson, E. Rumsey, M. Thorpe and R. K. Heenan, *J. Am. Chem. Soc.*, 2001, **123**, 988–989.

66 A. I. Cooper, J. D. Londono, G. Wignall, J. B. McClain, E. T. Samulski, J. S. Lin, A. Dobrynin, M. Rubinstein, A. L. C. Burke, J. M. J. Frechet and J. M. DeSimone, *Nature*, 1997, **389**, 368–371.

67 M. J. Hollamby, K. J. Trickett, A. Mohamed, S. Cummings, R. F. Tabor, O. Myakonkaya, S. Gold, S. Rogers, R. K. Heenan and J. Eastoe, *Angew. Chem., Int. Ed.*, 2009, **48**, 4993–4995.

68 J. Eastoe, A. Downer, A. Paul, D. C. Steytler, E. Rumsey, J. Penfold and R. K. Heenan, *Phys. Chem. Chem. Phys.*, 2000, **2**, 5235–5242.

69 J. Eastoe, S. Gold, S. Rogers, P. Wyatt, D. C. Steytler, A. Gurgel, R. K. Heenan, X. Fan, E. J. Beckman and R. M. Enick, *Angew. Chem., Int. Ed.*, 2006, **45**, 3675–3677.

70 K. P. Johnston, D. Cho, S. R. P. DaRocha, P. A. Psathas, W. Ryoo, S. E. Webber, J. Eastoe, A. Dupont and D. C. Steytler, *Langmuir*, 2001, **17**, 7191–7193.

71 M. J. Hollamby, K. Trickett, A. Vesperinas, C. Rivett, D. C. Steytler, Z. Schnepp, J. Jones, R. K. Heenan, R. M. Richardson, O. Glatter and J. Eastoe, *Chem. Commun.*, 2008, 5628–5630.

72 M. Anand, P. W. Bell, X. Fan, R. M. Enick and C. B. Roberts, *J. Phys. Chem. B*, 2006, **110**, 14693–14701.

73 P. W. Bell, M. Anand, X. Fan, R. M. Enick and C. B. Roberts, *Langmuir*, 2005, **21**, 11608–11613.

74 P. S. Shah, J. D. Holmes, R. C. Doty, K. P. Johnston and B. A. Korgel, *J. Am. Chem. Soc.*, 2000, **122**, 4245–4246.

75 J. B. McClain, D. Londono, J. R. Combes, T. J. Romack, D. A. Canelas, D. E. Betts, G. D. Wignall, E. T. Samulski and J. M. DeSimone, *J. Am. Chem. Soc.*, 1996, **118**, 917–918.

76 S. Cummings, D. Xing, R. Enick, S. Rogers, R. Heenan, I. Grillo and J. Eastoe, *Soft Matter*, 2012, **8**, 7044–7055.

77 K. Trickett, D. Xing, R. Enick, J. Eastoe, M. J. Hollamby, K. J. Mutch, S. E. Rogers, R. K. Heenan and D. C. Steytler, *Langmuir*, 2010, **26**, 83–88.

78 G. Gröger, W. Meyer-Zaika, C. Böttcher, F. Gröhn, C. Ruthard and C. Schmuck, *J. Am. Chem. Soc.*, 2011, **133**, 8961–8971.

79 J. H. Ortony, T. Chatterjee, L. E. Garner, A. Chworos, A. Mikhailovsky, E. J. Kramer and G. C. Bazan, *J. Am. Chem. Soc.*, 2011, **133**, 8380–8387.

80 V. Lebedev, L. Vinogradova and G. Török, *Macromol. Symp.*, 2010, **296**, 183–188.

81 H. Kumari, A. V. Mossine, S. R. Kline, C. L. Dennis, D. A. Fowler, S. J. Teat, C. L. Barnes, C. A. Deakyne and J. L. Atwood, *Angew. Chem., Int. Ed.*, 2012, **51**, 1452–1454.

82 H. Kumari, S. R. Kline, W. G. Wycoff, R. L. Paul, A. V. Mossine, C. A. Deakyne and J. L. Atwood, *Angew. Chem., Int. Ed.*, 2012, **51**, 5086–5091.

83 H. Kumari, S. R. Kline, W. G. Wycoff and J. L. Atwood, *Small*, 2012, **8**, 3321–3325.

84 G. M. Newbloom, F. S. Kim, S. A. Jenekhe and D. C. Pozzo, *Macromolecules*, 2011, **44**, 3801–3809.

85 G. M. Newbloom, K. M. Weigandt and D. C. Pozzo, *Macromolecules*, 2012, **45**, 3452–3462.

86 G. M. Newbloom, K. M. Weigandt and D. C. Pozzo, *Soft Matter*, 2012, **8**, 8854–8864.

87 D. B. Williams and C. B. Carter, *Transmission Electron Microscopy: A Textbook for Materials Science*, Springer, 2nd edn, 2009.

88 C.-Y. Chen, S.-H. Chan, J.-Y. Li, K.-H. Wu, H.-L. Chen, J.-H. Chen, W.-Y. Huang and S.-A. Chen, *Macromolecules*, 2010, **43**, 7305–7311.

89 J. Teixeira, *J. Appl. Crystallogr.*, 1988, **21**, 781–785.

90 F. G. Brunetti, R. Kumar and F. Wudl, *J. Mater. Chem.*, 2010, **20**, 2934–2948.

91 M. T. Dang, L. Hirsch and G. Wantz, *Adv. Mater.*, 2011, **23**, 3597–3602.

92 W. Yin and M. Dadmun, *ACS Nano*, 2011, **5**, 4756–4768.

93 H. Chen, S. Hu, H. Zang, B. Hu and M. Dadmun, *Adv. Funct. Mater.*, 2012, DOI: 10.1002/adfm.201202035, early view.

94 J. W. Kiel, A. P. R. Eberle and M. E. Mackay, *Phys. Rev. Lett.*, 2010, **105**, 168701.

95 M. Dadmun, *Phys. Chem. Chem. Phys.*, 2012, **14**, 5635–5641.

96 D. Chen, A. Nakahara, D. Wei, D. Nordlund and T. P. Russell, *Nano Lett.*, 2011, **11**, 561–567.

97 P. A. FitzGerald and G. G. Warr, *Adv. Colloid Interface Sci.*, 2012, **179–182**, 14–21.

98 K. Ito, *Curr. Opin. Colloid Interface Sci.*, 2010, **14**, 28–34.

99 S.-H. Choi, S. Lee, H. E. Soto, T. P. Lodge and F. S. Bates, *J. Am. Chem. Soc.*, 2011, **133**, 1722–1725.

100 C. V. Cerclier, M. Ndao, R. Busselez, R. Lefort, E. Grelet, P. Huber, A. V. Kityk, L. Noirez, A. Schönhals and D. Morineau, *J. Phys. Chem. C*, 2012, **116**, 18990–18998.

101 J.-H. Lee, S.-M. Choi, B. D. Pate, M. H. Chisholm and Y.-S. Han, *J. Mater. Chem.*, 2006, **16**, 2785–2791.

102 J. J. Vallooran, S. Bolisetty and R. Mezzenga, *Adv. Mater.*, 2011, **23**, 3932–3937.

103 J. M. McMullan and N. J. Wagner, *Soft Matter*, 2010, **6**, 5443–5450.

104 P. Sharifi, H. Eckerlebe and F. Marlow, *Phys. Chem. Chem. Phys.*, 2012, **14**, 10324–10331.

105 B. R. Pauw, M. E. Vigild, K. Mortensen, J. W. Andreasen and E. A. Klop, *J. Appl. Crystallogr.*, 2010, **43**, 837–849.

106 M. Granite, A. Radulescu and Y. Cohen, *Langmuir*, 2012, **28**, 11025–11031.

107 A. A. Golosova, J. Adelsberger, A. Sepe, M. A. Niedermeier, P. Lindner, S. S. Funari, R. Jordan and C. M. Papadakis, *J. Phys. Chem. C*, 2012, **116**, 15765–15774.

108 W. Zhou, M. Islam, H. Wang, D. Ho, A. Yodh, K. Winey and J. Fischer, *Chem. Phys. Lett.*, 2004, **384**, 185–189.

109 S. Fogden, C. A. Howard, R. K. Heenan, N. T. Skipper and M. S. P. Shaffer, *ACS Nano*, 2012, **6**, 54–62.

110 T. Chatterjee, A. Jackson and R. Krishnamoorti, *J. Am. Chem. Soc.*, 2008, **130**, 6934–6935.

111 D. W. Schaefer, J. Zhao, J. M. Brown, D. P. Anderson and D. W. Tomlin, *Chem. Phys. Lett.*, 2003, **375**, 369–375.

112 E. M. Milner, N. T. Skipper, C. A. Howard, M. S. P. Shaffer, D. J. Buckley, K. A. Rahnejat, P. L. Cullen, R. K. Heenan, P. Lindner and R. Schweins, *J. Am. Chem. Soc.*, 2012, **134**, 8302–8305.

113 C.-S. Tsao, M. Li, Y. Zhang, J. B. Leao, W.-S. Chiang, T.-Y. Chung, Y.-R. Tzeng, M.-S. Yu and S.-H. Chen, *J. Phys. Chem. C*, 2010, **114**, 19895–19900.

114 N. Hu, N. Borkar, D. Kohls and D. W. Schaefer, *J. Membr. Sci.*, 2011, **379**, 138–145.

115 K. M. Ford, B. G. Konzman and J. F. Rubinson, *Anal. Chem.*, 2011, **83**, 9201–9205.

116 L. M. Anovitz, D. R. Cole, G. Rother, L. F. Allard, A. J. Jackson and K. C. Littrell, *Geochim. Cosmochim. Acta*, 2013, **102**, 280–305.

117 S. Mazumder, D. Sen and A. K. Patra, *Pramana-J. Phys.*, 2004, **63**, 165–173.

118 M. Schoeffel, N. Brodie-Linder, F. Audonnet and C. Alba-Simionesco, *J. Mater. Chem.*, 2011, **22**, 557–567.

119 Z. Mileeva, D. K. Ross, D. Wilkinson, S. M. King, T. A. Ryan and H. Sharrock, *Carbon*, 2012, **50**, 5062–5075.

120 Z. H. Chen, C. Kim, X. Zeng, S. H. Hwang, J. Jang and G. Ungar, *Langmuir*, 2012, **28**, 15350–15361.

121 N. C. Gallego, L. He, D. Saha, C. I. Contescu and Y. B. Melnichenko, *J. Am. Chem. Soc.*, 2011, **133**, 13794–13797.

122 S. A. Samoylenko, S. E. Kichanov, D. P. Kozlenko, A. V. Belushkin, V. M. Haramus, E. A. Trusova, G. P. Shevchenko, V. S. Gurin, L. A. Bulavin, S. K. Rakhmanov and B. N. Savenko, *J. Phys.: Conf. Ser.*, 2012, **351**, 012017.

123 G. Choudhuri, S. Neogy, D. Sen, S. Mazumder, D. Srivastava, G. K. Dey and B. K. Shah, *J. Nucl. Mater.*, 2012, **430**, 205–215.

124 M. Laurent-Brocq, F. Legendre, M.-H. Mathon, A. Mascaro, S. Poissonnet, B. Radiguet, P. Pareige, M. Loyer and O. Leseigneur, *Acta Mater.*, 2012, **60**, 7150–7159.

125 H. Leitner, M. Bischof, H. Clemens, S. Erlach, B. Sonderegger, E. Kozeschnik, J. Svoboda and F. D. Fischer, *Adv. Eng. Mater.*, 2006, **8**, 1066–1077.

126 E.-W. Huang, J. Csiszár, Y.-C. Lo, Y.-L. Huang, W.-J. Lee, T. Ungár and P. K. Liaw, *Adv. Eng. Mater.*, 2012, **14**, 902–908.

127 J. W. Lynn, in *Characterization of Materials*, John Wiley & Sons, Inc., 2002.

128 Y. Oba, S. Koppoju, M. Ohnuma, T. Murakami, H. Hatano, K. Sasakawa, A. Kitahara and J. Suzuki, *ISIJ Int.*, 2011, **51**, 1852–1858.

129 R. Coppola, M. Klimenkov, R. Lindau, A. Möslang, M. Valli and A. Wiedenmann, *J. Nucl. Mater.*, 2011, **409**, 100–105.

130 M. R. Eskildsen, P. L. Gammel, B. P. Barber, A. P. Ramirez, D. J. Bishop, N. H. Andersen, K. Mortensen, C. A. Bolle, C. M. Lieber and P. C. Canfield, *Phys. Rev. Lett.*, 1997, **79**, 487–490.

131 P. L. Gammel, U. Yaron, A. P. Ramirez, D. J. Bishop, A. M. Chang, R. Ruel, L. N. Pfeiffer, E. Bucher, G. D'Anna, D. A. Huse, K. Mortensen, M. R. Eskildsen and P. H. Kes, *Phys. Rev. Lett.*, 1998, **80**, 833–836.

132 A. Pautrat, A. Brulet, C. Simon and P. Mathieu, *Phys. Rev. B: Condens. Matter Mater. Phys.*, 2012, **85**, 184504.

133 M. Ohnuma, J. Suzuki, S. Ohtsuka, S.-W. Kim, T. Kaito, M. Inoue and H. Kitazawa, *Acta Mater.*, 2009, **57**, 5571–5581.

134 Y. Oba, S. Koppoju, M. Ohnuma, Y. Kinjo, S. Morooka, Y. Tomota, J. Suzuki, D. Yamaguchi, S. Koizumi, M. Sato and T. Shiraga, *ISIJ Int.*, 2012, **52**, 457–463.

135 G. Eckold, H. Schober and S. E. Nagler, *Studying Kinetics with Neutrons: Prospects for Time-Resolved Neutron Scattering*, Springer, 2009.

136 J. L. Blin and M. Impéror-Clerc, *Chem. Soc. Rev.*, 2013, DOI: 10.1039/C2CS35362H, Advance Article.

137 R. F. Tabor, J. Eastoe and I. Grillo, *Soft Matter*, 2009, **5**, 2125–2129.

138 K. Bressel, M. Muthig, S. Prévost, I. Grillo and M. Gradzielski, *Colloid Polym. Sci.*, 2010, **288**, 827–840.

139 J. Gummel, M. Sztucki, T. Narayanan and M. Gradzielski, *Soft Matter*, 2011, **7**, 5731–5738.

140 E. L. Ferguson, E. De Luca, R. K. Heenan, S. M. King and P. C. Griffiths, *Macromol. Rapid Commun.*, 2010, **31**, 1685–1690.

141 V. Pipich, M. Balz, S. E. Wolf, W. Tremel and D. Schwahn, *J. Am. Chem. Soc.*, 2008, **130**, 6879–6892.

142 S. M. He, N. H. van Dijk, M. Paladugu, H. Schut, J. Kohlbrecher, F. D. Tichelaar and S. van der Zwaag, *Phys. Rev. B: Condens. Matter Mater. Phys.*, 2010, **82**, 174111.

143 C. Fernandez-Martin, G. Bruno, A. Crochet, D. Ovono Ovono, M. Comte and L. Hennet, *J. Am. Ceram. Soc.*, 2012, **95**, 1304–1312.

144 R. Motokawa, T. Taniguchi, Y. Sasaki, Y. Enomoto, F. Murakami, M. Kasuya, M. Kohri and T. Nakahira, *Macromolecules*, 2012, **45**, 9435–9444.

145 T. Terashima, R. Motokawa, S. Koizumi, M. Sawamoto, M. Kamigaito, T. Ando and T. Hashimoto, *Macromolecules*, 2010, **43**, 8218–8232.